Optomechanical characterisation of compressively prestressed silicon oxynitride films deposited by plasma-enhanced chemical vapour deposition on silicon membranes

M. Jozwik, P. Delobelle, C. Gorecki, A. Sabac, L. Nieradko, C. Meunier, F. Munnik

▶ To cite this version:

M. Jozwik, P. Delobelle, C. Gorecki, A. Sabac, L. Nieradko, et al.. Optomechanical characterisation of compressively prestressed silicon oxynitride films deposited by plasma-enhanced chemical vapour deposition on silicon membranes. Thin Solid Films, 2004, 468 (1-2), pp.84-92. 10.1016/j.tsf.2004.04.019 . hal-00096940

HAL Id: hal-00096940
https://hal.science/hal-00096940

Submitted on 14 Apr 2021

HAL is a multi-disciplinary open access archive for the deposit and dissemination of scientific research documents, whether they are published or not. The documents may come from teaching and research institutions in France or abroad, or from public or private research centers.

L'archive ouverte pluridisciplinaire **HAL**, est destinée au dépôt et à la diffusion de documents scientifiques de niveau recherche, publiés ou non, émanant des établissements d'enseignement et de recherche français ou étrangers, des laboratoires publics ou privés.

Distributed under a Creative Commons Attribution 4.0 International License

Optomechanical characterisation of compressively prestressed silicon oxynitride films deposited by plasma-enhanced chemical vapour deposition on silicon membranes

M. Józwik[a,b], P. Delobelle[c], C. Gorecki[a,*], A. Sabac[a], L. Nieradko[a], C. Meunier[d], F. Munnik[e]

[a] *Laboratoire d'Optique P.M. Duffieux (UMR CNRS 6603), Université de Franche-Comté, 16 Route de Gray, 25030 Besançon Cedex, France*
[b] *Institute of Micromechanics and Photonics, Warsaw University of Technology, Św. A. Boboli 8 St., 02-525 Warsaw, Poland*
[c] *Laboratoire de Mécanique Appliquée R. Chaléat (UMR CNRS 6604), Université de Franche-Comté, 24 rue de l'Epitaphe, 25000 Besançon Cedex, France*
[d] *Centre de Recherches sur les Ecoulements Surfaces et Transferts (UMR CNRS 6000), Université de Franche-Comté, 4 place Tharradin, 25200 Montbéliard Cedex, France*
[e] *Centre d'Analyses par Faisceau Ionique, 8A rue Jambe Ducommun, 2400 Le Locle, Switzerland*

Abstract

We have studied the composition and physical properties of silicon oxynitride (SiO_xN_y) films grown on silicon membranes by means of plasma-enhanced chemical vapour deposition (PECVD process). The influence of these properties on the mechanical behaviour of PECVD deposited films is investigated by an original "point-wise" deflection method. This technique, particularly appropriate for determining the residual stress in the case of prestressed membranes, is operating at the first order of buckling. It combines the classical interferometry with the nanoindentation technique. The interferometry measures the out-of-plane displacements of membranes with SiO_xN_y layers of different optical quality, while the nanoindentation permits the extraction of micromechanical properties such as hardness and Young's modulus. From the "point-wise" deflection technique, the distribution of residual stress was monitored as a function of the refractive index of SiO_xN_y films, establishing the correlation between the optical and micromechanical properties of deposited thin films. High measuring accuracy and resolution have been demonstrated, allowing the measurements to be used to enhance PECVD process control.

Keywords: PECVD process; Silicon oxynitride; Buckled membrane; Optical properties; Stress evaluation

1. Introduction

The tendency towards continuous miniaturisation of microelectromechanical systems (MEMS) is a further challenge to the thin films in use [1]. Optical waveguides may be integrated with MEMS structures such as beams, bridges and membranes. In such micro-optoelectromechanical systems (MOEMS), the waveguide can play the role of a sensor to detect a physical parameter of mechanical deformation. Such optomechanical structure is fabricated using bulk micromachining, where a number of different thin films is deposited on top of the silicon wafer, and the desired microstructures are obtained by successive deposition, etching and patterning operations on the surface of the wafer. The fabrication process induces additional internal and thermal stresses between different materials and strongly influences the mechanical behaviour and long-term performance of such microparts. For these reasons, easy, nondestructive and high-resolution measurement of micromechanical properties is crucial for optimising the design and defining the process control of MOEMS devices. Various mechanical techniques have been proposed to evaluate the simple properties such as Young's modulus, residual stress, strain and Poisson's ratio in the material [2–4]. Implementing of these methods is difficult in the case of thin film materials, and the reported values of micromechanical parameters vary widely, demonstrating that the

* Corresponding author. Tel.: +33-03-816-66607; fax: +33-03-8166-6423.
E-mail address: christophe.gorecki@univ-fcomte.fr (C. Gorecki).

measurement accuracy is not enough to provide high-confidence testing tools. Thus, the reported values of Young's modulus for polysilicon have ranged from 120 to 201 GPa. The potential of nondestructive optical techniques was also demonstrated in the determination of local material properties and dynamic investigation of MEMS/MOEMS. The efficiency of conventional or phase-shifting interferometry [5], holographic interferometry and digital holography [6], white light stroboscopic interferometry [7], speckle interferometry [8] and electronic speckle pattern interferometry [9] has been demonstrated.

Plasma-enhanced chemical vapour deposition (PECVD)-grown SiO_xN_y films can be applied as a core layer for channel waveguides [10,11]. However, the use of PECVD is still limited here because the residual stress of deposited films is difficult to control, and there is a limited understanding of film properties. In particular, the evaluation of mechanical parameters from compressively prestressed membranes suffers from absence of validated mechanical models. In order to improve this situation, we have firstly studied the material structure and composition of PECVD silicon oxynitride films by Rutherford backscattering spectroscopy (RBS), elastic recoil detection analysis (ERDA) and X-ray reflectivity (XRR). Secondly, we reported the influence of these properties on the mechanical behaviour of PECVD SiO_xN_y films. For this purpose, the evaluation of mechanical parameters is performed in case of buckling membranes prestressed by PECVD-grown SiO_xN_y layers of different optical quality. To determinate the stress in SiO_xN_y layers, a special technique was developed based on the bending principle of this membrane. The measurement of out-of-plane deformations of the center of membrane, generated by the compressive stress, is performed by interferometry. To extract residual stress, the interferometric data are combined with micromechanical parameters obtained by means of nanoindentation test [12]. The correlation between the micromechanical properties and refractive index of SiO_xN_y thin films is established carefully. We compare our results with those reported in literature.

2. Experimental study of physical parameters of SiO_xN_y thin films

2.1. PECVD deposition of SiO_xN_y films

SiO_xN_y films were fabricated by a parallel plate PECVD, radial flow reactor (PLASSYS MPC 400). Three processing gases, silane (SiH_4), ammonia (NH_3) and nitrous oxide (N_2O), are supplied from individual flow control systems inside the reactor chamber. The substrate temperature during the deposition is 350 °C; RF power is fixed at 0.11 W/cm^2, RF frequency at 150 kHz and the pressure at 0.14 mbar for a total gas flow of 150 sccm (flow unit defined as "standard cm^3 per min"). Under these conditions, all SiO_xN_y samples were prepared varying only the gas flow ratio of N_2O and NH_3. When the ratio $R = N_2O/(N_2O + NH_3)$ is varying from 0 to 1, the refractive index of the SiO_xN_y is adjusted from 1.815 to 1.469. Letters a, b, c, d, e and f denote SiO_xN_y samples for which the deposition parameters are listed in Table 1. The refractive index of the samples was measured by a Gaertner L117 ellipsometer, operating at a wavelength of 632.8 nm.

2.2. Methods of SiO_xN_y films characterisation

Samples a–f were analysed within a Van der Graaff accelerator using an RBS detector ERDA system. A 2 MeV He^+ beam was generated with an angle between sample normal and incoming beam of 76° and the analysis spot size is 0.5×0.5 mm^2. The scattered ions were detected with charge-sensitive "surface barrier" detectors at an angle of 150° for RBS and 20° for ERDA. An additional RBS measurement with a sample angle of −30° has also been performed, and for sample a, RBS measurement with 2 MeV protons has been done. RBS with two different sample angles was used to obtain information on the composition and thickness. ERDA was used to obtain the depth profile for hydrogen. We used an XRR system to determine electronic densities of SiO_xN_y films, using a Philips X'Pert MPD equipment. Experimental data are summarised in Table 2 where the film thickness, the atomic percent of silicon, nitrogen, oxygen and hydrogen, and mass density of deposited films with various refractive indexes are given.

For samples (a, b, d, e, f) of SiO_xN_y, the etch rate is measured in a mixture for isotropic etching of HF (50%):HNO_3 (69%):H_2O with a volume ratio of 9:75:50, operating at room temperature.

2.3. Methodology of SiO_xN_y membrane fabrication

Five sets of square (3.6×3.6 mm^2) SiO_xN_y membranes were fabricated, as shown in Fig. 1 [13]. Firstly, both sides of a double-polished ⟨100⟩ silicon wafers was thermally oxided at the temperature of 1050 °C to grow 1-μm-thick layer of oxide. Square mask aligned in ⟨110⟩ direction was patterned by photolithography on the topside of the wafer. Then, the oxide layer was removed in buffered HF etch. The silicon substrate from which the oxide layer has been

Table 1
Refractive index of the samples versus the ratio N_2O to $N_2O + NH_3$ flow rates

Sample	R=(N_2O)/($N_2O + NH_3$)	N_2O [sccm]	SiH_4 [sccm]	NH_3 [sccm]
a	1	143	7	0
b	0.88	126	7	17
c	0.60	86	7	57
d	0.32	46	7	97
e	0.11	17	7	126
f	0	0	7	143

Table 2
Atomic percent of Si, N, O and H and mass density

Sample	Refractive index n	Thickness [nm]	Si [at.%]	N [at.%]	O [at.%]	H [at.%]	Mass density [g/cm^3]
a	1.469	116.8	32.4	0	65.6	2.0	2.290
b	1.517	151.6	31.7	10.9	53.8	3.6	2.440
c	1.573	115.2	29.6	19.5	44.3	6.6	2.365
d	1.645	100.6	30.1	28.0	30.0	11.9	2.435
e	1.700	107.2	30.8	35.2	17.5	16.5	2.520
f	1.815	90	29.1	52.1	0	18.8	2.710

removed was anisotropically etched by a KOH solution, giving a 15-μm-thick membrane. After photoresist stripping on the topside of the wafer, the oxide layers were removed from both sides. Finally, 2-μm-thick SiO_xN_y films were deposited by PECVD on the backside of the wafer, operating under PECVD conditions described in Section 2.1. In the following sections, letters B, C, D, E, F denote the range of refractive index for each set of SiO_xN_y prestressed membranes.

2.4. Evaluation of mechanical properties of SiO_xN_y thin films

In this section, Young's modulus and residual stress state of SiO_xN_y of membranes with different optical quality are characterised with the following investigations: (a) estimation of micromechanical properties of membranes (Young's modulus, hardness) by nanoindentation tests; (b) evaluation of residual stress by means of membrane "point-wise" deflection method using the interferometry; and (c) analysis by means of finite element method (FEM).

2.4.1. Methodology of nanoindentation test

To measure the Young's modulus and hardness of PECVD-grown SiO_xN_y membranes, we applied the indentation tip of Nano-Indenter IIs on the bulk part of a sample containig 2-μm thick SiO_xN_y film on top of 380-μm-thick silicon substrate. The tip is applied during the well-controlled loading–unloading cycles. The applied load P of the indenter is measured as a function of his penetration depth h, delivering the "load–displacement curve" from which Young's modulus E and the hardness H of sample are calculated [14,15]. In addition, we used the "continuous contact stiffness method", where the penetration of the indenter tip into the sample is accompanied by 1 nm amplitude vibration of the tip performed at the frequency of 45 Hz [15]. This permits to follow the variations of Young's modulus E and hardness H as a function of indentation depth. The maximum depth of indentation is fixed at 900 nm and 15 indents are performed for each of five samples on the test area of 300×300 μm^2.

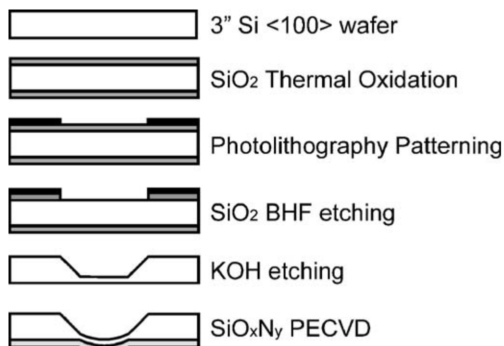

Fig. 1. Fabrication of SiO_xN_y membranes.

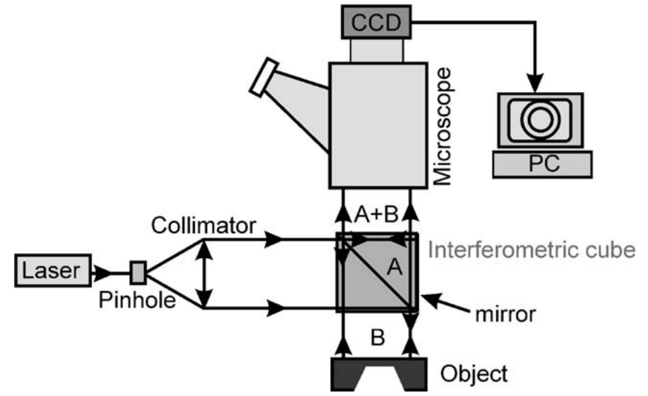

Fig. 2. Schematic view of the interferometric system.

2.4.2. Methodology of deflection measurement by interferometry

The compressive buckling due to PECVD deposition produces an initial deflection h_0. To measure h_0 at the center of SiO_xN_y membranes, we used an interferometric technique, shown in Fig. 2 [16]. This is based on a metallurgical Nikon microscope where a Twyman–Green interferometer (TGI) is inserted between the sample to be measured and the microscope objective. TGI consists of a cube beamsplitter where one of beamsplitter facets is metal overcoated, playing the role of the reference mirror of the interferometer. The sample is illuminated by a He–Ne laser beam ($\lambda = 632.8$ nm) obtained by a spatial filter and directed through a collimating lens to the cube beamsplitter. Both the reference and measuring arms produce interference patterns. Five interferograms with $\pi/2$ relative phase shifts between the measuring and reference wavefronts are acquired and visualised by a 768×576 CCD array coupled with a frame grabber and then was analysed by automatic fringe pattern analyser [17]. Once continuous phase distribution $\Phi(x,y)$ is evaluated, the corresponding out-of-plane displacement $h_0(x,y)$ is calculated with inaccuracy within 10 nm.

3. Theory behind the FEM analysis of the optomechanical evaluation of residual stress

The principle of stress evaluation in thin films is based on the measuring the point-wise deflection at the membrane center. The nanoindenter tip is applied on the membrane

with increased load P, and deflection h produced by the tip is monitored. This permits the calculation membrane stiffness $S = \mathrm{d}P/\mathrm{d}h$. Therefore, knowing the Young's modulus and Poisson ratio, as well as the analytical relationship between the load P to the membrane deflection h, the presence of residual stress, the average value of stress is extracted. The efficiency of "point-wise" deflection techniques, less widely used that than the bulging test [18–21], was demonstrated in case of tensile membranes [12,22], where the membrane is not fixated by fluid-tight or airtight gluing on a rigid support, modifying the state of residual stress. However, the interpretation of experimental results, obtained by deflection method on compressively prestressed materials, such as of SiO_xN_y films, is difficult because the absence of theoretically validated models. Consequently, we report here the experimental results accompanied by the theoretical study as well as the modeling data obtained by finite element method (FEM).

Interferometric data demonstrated that the square SiO_xN_y membranes are operating at the first mode of buckling (Fig. 3). In this case, the theoretical deformation at first approximation is [23]:

$$h = -\frac{h_0}{4}\left(1 - \cos\frac{2\pi x}{a}\right)\left(1 - \cos\frac{2\pi y}{a}\right) \tag{1}$$

where a is the size of the membrane. A more accurate second-order relation was reported by Maier-Sneider et al. [24].

3.1. Theoretical study of the relation P=f(h) in case of bimorph membranes

In the case of bimorph membranes, an isotropic material, such as a SiO_xN_y, is grown on top of anisotropic $\langle 100 \rangle$ substrate of silicon, generating an internal stress of compressive or tensile nature. When the magnitude of stress attain the value of critical stress of buckling, the bimorph structure presents an initial curvature. If the exact analytical solution of this problem is impossible for square membranes, the analytical solutions can by calculated by FEM in case of circular geometry. This last solution can be then extended to the case of square geometry. It was reported [23] that the point deflection at the center of a square membrane containing one material is:

$$P = \frac{D}{\alpha a^2}h + C\left(v, \frac{h}{e}\right)\frac{Ee}{a^2}h^3 \quad \text{with} \quad D = \frac{Ee^3}{12(1 - v^2)} \tag{2}$$

where D is the bending moment, E and v are Young's modulus and Poisson's ratio, e is the membrane thickness, $\alpha = 5.6 \times 10^{-3}$ is a parameter for square membranes, and C is a function of v and h/e calculated by FEM. For small values of h/e, we have $C = 6.1/(1 - v^2)$ [23]. For small deflections with $h/e < 0.3$, the function $P = f(h)$ is linear. When the deflection is several times higher than the membrane thickness, $P = f(h)$ follows a cubic law.

In the case of bimorph membranes, the effective parameters D_{eff}, E_{ff}, and e_{eff} are defined. For anisotropic materials, D_{eff} becomes a function of the bending moments $D_{x\mathrm{eff}}$, $D_{y\mathrm{eff}}$ and $H_{xy\mathrm{eff}}$, these bending moments depending from the elastic constants C_{ij} and crystallographic orientations of material. For the membranes of circular geometry with uniform distribution of stress σ_0, a "stress function" $g(k_0)$ is defined. This function is defined for circular membranes of radius a in both tensile or compressive situations. Then, the solutions will be recalculated by FEM for square geometry of membrane with:

$$k_0^2 = \frac{Na^2}{D_{\mathrm{eff}}} \quad \text{with} \quad N = \sigma_{\mathrm{f}}e_{\mathrm{f}} + \sigma_{\mathrm{s}}e_{\mathrm{s}} = \sigma_{\mathrm{eff}}(e_{\mathrm{f}} + e_{\mathrm{s}}) \tag{3}$$

where N is the radial force applied by unit of length and linking the substrate stress σ_{s} with film stress σ_{f}, and σ_{eff} represents the effective stress.

In the case of tensile stress [12,22], we have:

$$g(k_0) = \frac{8}{k_0^2}\left[\frac{K_1(k_0) - \frac{1}{k_0}}{I_1(k_0)}(I_0(k_0) + 1) + K_0(k_0) + \ln\frac{k_0}{2} + \gamma\right]. \tag{4}$$

In the case of compressive stress, we obtain:

$$g(k_0) = \frac{8}{k_0^2}\left[\frac{\frac{\pi}{2}Y_1(k_0) + \frac{1}{k_0}}{J_1(k_0)}(1 - J_0(k_0)) + \frac{\pi}{2}Y_0(k_0) - \ln\frac{k_0}{2} - \gamma\right]. \tag{5}$$

K_0/K_1 are Bessel functions of the second kind of orders 0/1, I_0/I_1 are the modified Bessel functions of the first kind of orders 0/1, γ represents the Euler's constant, Y_0/Y_1 are

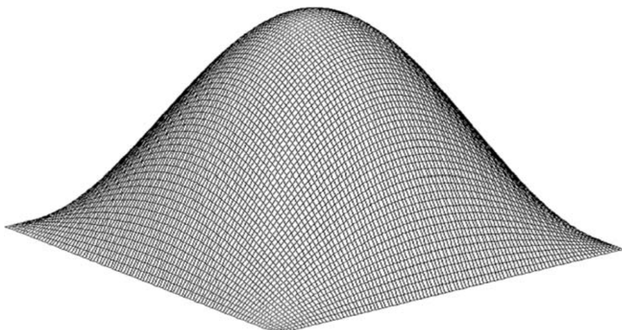

Fig. 3. Shape of a square membrane at the first mode of buckling.

the Bessel functions of the first kind of orders 0/1 and J_0/J_1 are the Bessel functions of the second kind of orders 0/1.

In compressive situation, the first zero of the function $J_1(k_0)$ is equal to the value k_0^{cr} of the critical stress of buckling. The $g(k_0)$ is plotted in Fig. 4, where the different branches represents three situations of stress: (a) tensile stress with $\sigma_{eff}>0$ and $0<g(k_0)<1$; (b) compressive stress before the buckling with $\sigma_{eff}<0$ and $1<g(k_0)<\infty$; and (c) buckling regime of membrane for $\sigma_{eff}<0$ and with $-\infty<g(k_0)<0$. A FEM modeling of these functions was performed on circular and square membranes, as shown in Fig. 4, where the calculation results are reported with circular or square symbols. Excepted for high values of k_0 around $g(k_0)=0$, there is a good agreement with analytical data. Around $g(k_0)=0$, FEM model is not working.

In conclusion, the analytical solution of $g(k_0)$ is validated for small deflections, while for the strongest values of k_0, the analytical solution is not applicable because the buckling produces an initial deflection of membranes that can be above the membrane thickness. The transposition of these results in the case of square membranes requires the introduction of corrective factor on the parameter k_0. This is calculated by FEM modeling and validated in both compressive and tensile [19] situations (see Fig. 4):

$$k_0\ (\mathrm{sq}) = \frac{2k_0\ (\mathrm{cir})}{1.07} \tag{6}$$

where the correction is 7%; the factor "2" takes into account fact that a is now the radius of circular membranes (for square membranes, a is the side of a square). This correction is confirmed on the calculated data of critical buckling:

$$k_0^{cr}\ (\mathrm{cir}) = 3.83, \quad k_0^{cr}\ (\mathrm{sq}) = \frac{4\pi}{\sqrt{3}}, \quad \text{thus}$$
$$k_0^{cr}\ (\mathrm{sq}) = \frac{2k_0^{cr}\ (\mathrm{cir})}{1.06}. \tag{7}$$

In the absence of initial stress ($k_0=0$), and for small deflections ($h/e=0.8$), the coefficient $C(v,h/e,k_0)$ is respectively calculated by FEM for both circular and square membranes:

$$C\ (\mathrm{cir})(v,0,0) = \frac{1.87}{1-v^2} \quad \text{and}$$
$$C\ (\mathrm{sq})(v,0,0) = \frac{4C\ (\mathrm{cir})}{1.23(1-v^2)} = \frac{6.1}{1-v^2}. \tag{8}$$

The first equation corresponds to the analytic solution given by Timoshenko and Woinowsky-Krieger [23]. The correction factor for square membranes here is 23%. For strong deflections (until $h/e \approx 7$), C decreases with h/e and the adjustment of FEM results by an analytic function is made for square membranes with:

$$C\ (\mathrm{sq})\left(v,\frac{h}{e},0\right) = \frac{6.1}{1-v^2}\left[1-0.47 \times \left(1-\exp-0.168\frac{h}{e}\right)\right]. \tag{9}$$

For bigger deflections ($h/e \gg 1$), C is constant: C (sq)= $(3.23)/(1-v^2)$.

C is a function of k_0 for both compressive and tensile stress. Until the value of the limit stress of buckling the influence of k_0 on C is negligible. This approach permits the applicability of "point-wise" deflection technique to ⟨100⟩ silicon membranes of square geometry with PECVD-grown SiO_xN_y. Eq. (2), linking the applied load P at the center of membrane with the out-of-plane displacement h, becomes:

$$\frac{P}{h} = \frac{A}{g(k_0)} + BC\left(v,\frac{h}{e},0\right)h^2 \quad \text{with}$$
$$A = \frac{D_{eff}}{\alpha a^2} \quad \text{and} \quad B = \frac{E_{eff}e_{eff}}{a^2}. \tag{10}$$

The zero of the linear function $P/h=f(h^2)$ and the knowledge of D_{eff} permit the determination of $g(k_0)$ and k_0, and finally, the extraction of σ_{eff} and σ_f (Eq. (3)). There are four following solutions: (a) $P/Ah=1$ with $g(k_0)=1$ in the absence of stress; (b) $P/Ah>1$ with $0<g(k_0)<1$ in tensile situation; (c) $0<P/Ah<1$ with $g(k_0)>1$ in the presence of compressive stress before buckling; and (d) $P/Ah<0$ with $g(k_0)<0$ in the presence of compressive stress of magnitude greater than the value of critical stress of buckling σ_0^{cr}. The monitoring the function C (Eq. (9)) permits to extract E_{eff} and E_f by determination of the slope of function P/h (Eq. (10)). When $k_0>k_0^{cr}$, the deflection generated by compressive stress can be bigger than membrane thickness ($h_0>e$). In this case, the tensile stress can appear when applying the "point-wise" deflection technique. Therefore, we determine experimentally the values of k in the range $k \leq k_0$.

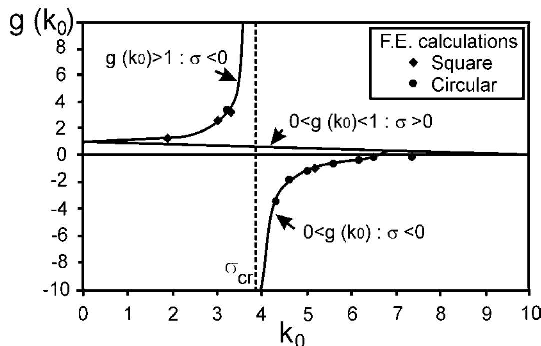

Fig. 4. Plot of the function $g(k_0)$.

When the membrane presents an initial bending h_0 due to the buckling, it is necessary to make a translation on the displacement h [19]. Eq. (10) becomes:

$$\frac{P}{h+h_0} = \frac{A}{g(k)} + BC\left(v, \frac{h}{e}, 0\right)(h+h_0)^2 \text{ with}$$

$$k^2(cir) = k_0^2(cir) - 9.7\left\langle \frac{h_0}{e} - 0.8 \right\rangle^2 \tag{11}$$

where function $g(k)$ is obtained by combining interferometric data of the initial bending h_0 and linear representation of Eq. (11); $\langle - \rangle$ are a Mac Cawley brackets.

4. Results and discussion

4.1. Properties of SiO_xN_y films

Experimental data of chemical composition are summarised in Table 2 where the film thickness, the atomic percent (at.%) of silicon, nitrogen, oxygen and hydrogen, and mass density of deposited films with various refractive indexes are given. Atomic concentrations were calculated from the layer thickness obtained in the analysis in units of atom/cm^2 [25]. Table 2 shows that the quantities of incorporated nitrogen increase (0–52%) with increasing refractive index, while the quantities of oxygen decrease (65–0%) with increasing refractive index. The silicon content (29–32%) is relatively independent of the refractive index. Hydrogen has particularly important effect on the mechanical and optical properties of deposited films: the atomic percentage increases rapidly (2–18.8%) with increasing refractive index. Solid line at Fig. 5 displays the atomic densities as a function of refractive index. The experimental data reveal a relatively linear increase in density with increasing refractive, accompanied by a jump for the sample b ($n = 1.517$). The oxide-like film (sample a, $n = 1.469$) has a density slightly upper than fused silica with 2.29 g/cm^3. The nitride-like film (sample f, $n = 1.815$) has the higher density with 2.70 g/cm^3. It will be shown later that denser films result in more compressive stress.

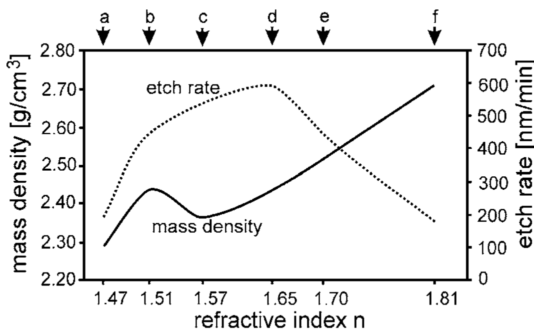

Fig. 5. Atomic densities of SiO_xN_y films and variation of etch rate versus the refractive index of samples (a–f).

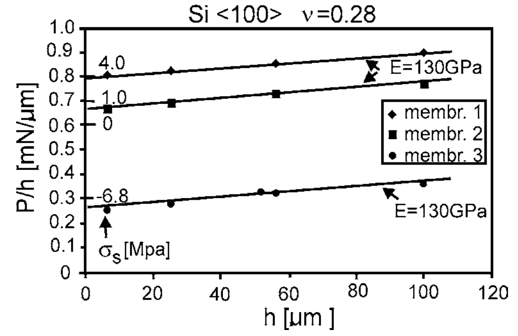

Fig. 6. Plot of the function P/h versus $f(h^2)$ in case of Si membrane.

The variations of etch rate with the evolution of the SiO_xN_y refractive index is represented by dashed line in Fig. 5. For the refractive index of 1.645 (sample d), the atomic percentages of oxygen and nitrogen are equivalent and then the atomic percentage of nitrogen becomes higher than the percentage of oxygen. The etch rate evolution follows this tendency, increasing from sample a to sample d ($n = 1.469$–1.645) where the etch rate is maximal, and then decreasing with increasing refractive index. We can conclude that the oxygen/nitrogen content influences the etch rate rather than hydrogen content.

4.2. Mechanical properties of SiO_xN_y membranes

To measure Young's modulus E_s of the substrate in the absence of initial stress, we first investigated the behavior of $\langle 100 \rangle$ silicon membranes ($a = 3.6$ mm, $e_s = 15$ μm) without SiO_xN_y layer. A deflection of 10 μm was produced by the nanoindenter on a series of membranes, as shown in Fig. 6 illustrating the Eq. (11) when $h_0 = 0$. The magnitude of stress was determined of these membranes is low: $\sigma_s = 1$, 4 and -6 MPa, and the measured Young's ($E_s = 130 \pm 4$ GPa when $\nu = 0.28$) is perfectly matched with calculated one ($E_x = E_y = E_s = 129$ GPa). For $\sigma_s \approx 0$ and $E_s = 129$ GPa, we can define σ_f in bimorph situation as:

$$\sigma_f \approx \sigma_{eff}\left(1 + \frac{e_s}{e_f}\right). \tag{12}$$

In the second step, we investigated the bimorph membranes with evaluation of Young's modulus. Fig. 7 shows

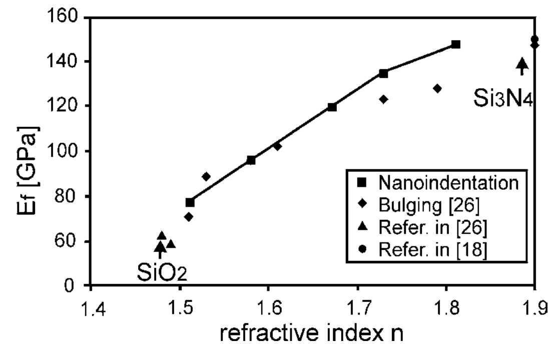

Fig. 7. Young's modulus versus the refractive index of SiO_xN_y film.

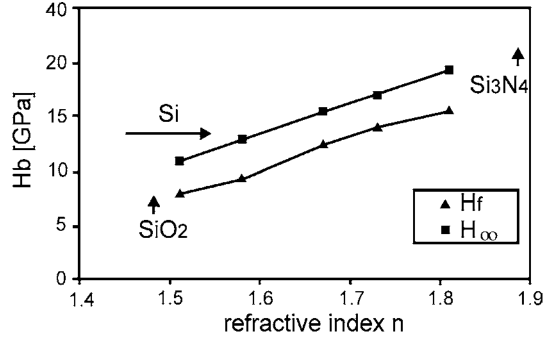

Fig. 8. Hardness H_f ($h \rightarrow 0$) and H_∞ ($h \rightarrow 900$ nm) versus the refractive index of SiO_xN_y film.

the quasi linear increase of Young's modulus as a function of refractive index of SiO_xN_y films. We have seen that the refractive index n increases linearly following the changes in the concentration of oxygen and nitrogen, according the modifications of gas flow ratio $R = N_2O/(N_2O + NH_3)$. The evolution of E_f as a function of n is in agreement with this linear law. For oxide-like films (series B, $n = 1.51$) the Young's modulus (78 GPa) is closed to the modulus of the thermal oxide (70 GPa), while for the nitride-like film (series F, $n = 1.81$), the Young's modulus (148 GPa) is close to the modulus of pure Si_3N_4 [26]. The measured values are in good agreement with the literature data [26,27].

By analogy with the behaviour of Young's modulus, both hardness values H_f (value of H for $h \rightarrow 0$) and H_∞ (value of H for $h = 900$ nm) increase linearly with the refractive index of SiO_xN_y films, as shown in Fig. 8.

Finally, the initial deflection h_0 of membranes was measured by interferometry. Fig. 9 shows the distribution of out-of-plane displacement h_0 versus the refractive index of the SiO_xN_y films for series B, C, D, E and F. The curve presents a minimal bending ($h_0 \approx 0$) for the refractive index $n = 1.58$ (series C). After that optimum, the deflection is increasing with the increase of the refractive index.

4.3. Comparison of experimental results with theoretical analysis

The representation of Eq. (11) in case of bimorph membranes is given in Fig. 10, where three categories of samples are shown (two membranes by class of series C, E and four for the F). The knowledge of h_0, E_s, v_s, E_f and v_f permits to follow the variation of σ_s as a function of refractive index. In addition, the values of E_{eff} can be estimated and compared with the theoretical calculation. For each class of samples with same refractive index, the straight lines of Fig. 10 crosses the same origin on the vertical axis, even presenting different slopes due to the dispersion of h_0 values. Consequently, the function $g(k)$ has the same value for each category of sample with same σ_{eff}. The standard deviation of σ_f is low. On the other hand, the variation of individual slopes depends strongly from the values of h_0, introducing a significant dispersion of E_{eff} results. The comparison of experimental and theoretical results is given in Table 3.

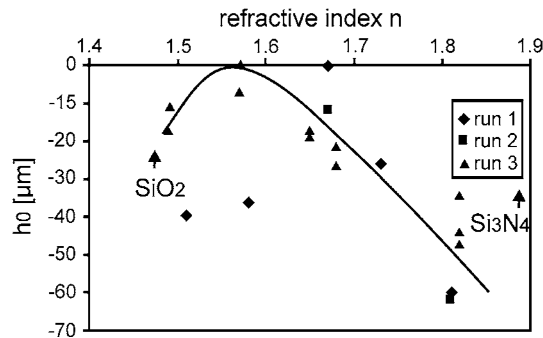

Fig. 9. Initial deflections h_0 versus the refractive index of SiO_xN_y film.

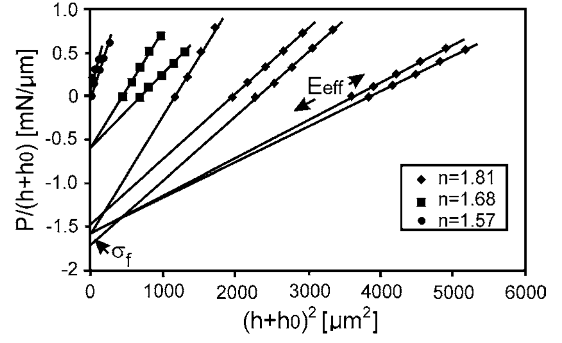

Fig. 10. Plot of the function $P/(h + h_0)$ versus $f((h + h_0)^2)$ in the case of bimorph membranes.

The distribution of residual stress σ_f versus the refractive index of SiO_xN_y thin films is shown in Fig. 11. This graph gives the fitting curve for averaged experimental data. In Table 3, deflections h_0 with sign «+» means a stress of tensile nature in the film of the buckled membrane. This is

Table 3
Values of h_0, $g(k)$, σ_f, E_{eff} and σ_f^{cr} versus the refractive index of SiO_xN_y film

Series	h_0 [µm]	$g(k)$	σ_f [MPa]	E_{eff} measured [GPa]	E_{eff} theoretic [GPa]	σ_f^{cr} [MPa]
B ($n = 1.49$–1.51)	≈ 10.7$^+$	− 3.31	− 119	219	122.8	− 98.0
	17.3	− 2.45	− 132	115	122.8	− 98.0
C ($n = 1.57$–1.58)	40	− 1.11	− 184	48	123.4	− 99.3
	0	+ 5.78	− 84	–	125.1	− 103
	6.6$^+$	− 13.8	− 106	310	125.1	− 103
	36	− 0.79	− 237	92	125.4	− 103
D ($n = 1.65$–1.67)	18.8	− 3.62	− 132	80	127.6	− 107.5
	17.1	− 3.15	− 135	98	127.6	− 107.5
	0*	+ 0.83	+ 16.1	–	128.2	− 108.6
	11.7	− 3.66	− 130	173	128.2	− 109.6
E ($n = 1.69$–1.73)	26.4	− 1.26	− 187	110	128.4	− 109
	21.3$^+$	− 1.23	− 189	171	128.4	− 109
	26	− 0.94	− 227	153	129.8	− 112
F ($n = 1.81$–1.82)	60	− 0.49	− 414	67	131.3	− 114.2
	62	− 0.49	− 414	68	131.3	− 114.2
	44	− 0.48	− 396	112	131.7	− 115.1
	47.8$^+$	− 0.46	− 452	108	131.7	− 115.1
	34	− 0.49	− 414	132	131.7	− 115.1

Comparison of theoretical and the experimental values of E_{eff}.

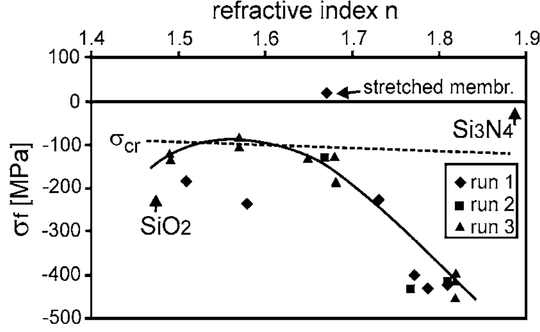

Fig. 11. Distribution of residual stress versus the refractive index of the SiO_xN_y film.

due to the passage of certain membranes from the compressive situation (convex membrane) to the tensile one (concave membrane) during the sample removing from PECVD furnace (passage from vacuum to the ambient air). The term «*» describes the membranes whose border was clamped mechanically during the measurement session. Consequently, a very low tensile stress ($\sigma_f = +16.0$ MPa) is measured (instead of compressive one in the range of -130 MPa). This demonstrates clearly the strong consequences of mechanical clamping of the sample on the stress evaluation. When the refractive index is increasing, the minimal stress is obtained for $n = 1.58$ with $\sigma_f = -100$ MPa, as shown in Fig. 11. We have seen that around this refractive index (sample C), the film density is lower. For nitride-like films, the stress becomes more compressive, increasing with the increase of refractive index. This attains -400 MPa around $n = 1.81$. On this graph, the evolution of the critical film stress of buckling is plotted:

$$\sigma_f^{cr} \approx \sigma_{eff}^{cr}\left(1 + \frac{e_s}{e_f}\right) \quad \text{with} \quad \sigma_{eff}^{cr} = \frac{16\pi^2}{3}\frac{D_{eff}}{e_{eff}a^2}. \tag{13}$$

For the series C ($n = 1.58$) where $g(k_0) > 0$, the measured stress is lower than the critical stress of buckling ($\sigma_f < \sigma_f^{cr}$). This is accompanied by a very low initial deflection h_0. Other samples lead to the buckling of bimorph structures with $g(k_0) < 0$. In conclusion, the optimal situation of SiO_xN_y deposition when the stress is of compressive nature and the membrane in the state of prebuckling is obtained for $n = 1.58$ (series C).

5. Concluding remarks

In this paper, an optomechanical approach of characterisation the mechanical performances of SiO_xN_y films has been demonstrated for the particular case of compressively prestressed silicon membranes by deposition of SiO_xN_y films. All SiO_xN_y films that we fabricated by PECVD process, operating at the temperature of 350 °C and obtained with low hydrogen content, are of compressive nature. Danaie et al. [28] reported that SiO_xN_y membranes with tensile stress can also be fabricated at low-frequency PECVD reactor when the thin film is deposited with higher hydrogen content and annealed after deposition to reduce the hydrogen content.

Table 4 shows an overview of measured values from the literature compared with the results of our contribution. SiO_xN_y layers are obtained from PECVD reactors operating with $SiH_4-NH_3-N_2O$ gas mixture. We can see a clear tendency concerning the magnitude of Young's modulus. Thus, Danaie et al. [28] measured the Young's modulus between 86 and 149 GPa within the range of refractive indices between 1.48 and 1.9, while Kramer and Paul [18] obtained 150 GPa for a refractive index above 2. This is in agreement with our estimation of the Young's modulus covering the range from 78 to 147 GPa for refractive indices within 1.51–1.81. The direct comparison is less evident concerning the residual stress magnitude because of the large number of processing parameters and the use of different PECVD reactors, although these estimations were made from measurements on membranes or on wafers. In the meantime, certain trends can be seen from the stress data. All deposited films were found to have a compressive stress. Our results are in agreement with estimation reported by Denisse et al. [29], demonstrating a similar level of compressive stress (240 to 310 versus 90 to 400 MPa for similar range of refractive index 1.5 to 1.7 versus 1.49 to 1.81). These results are confirmed by Kramer and Paul [18] that measured the compressive stress of 320 MPa for a refractive index above 2. Danaie et al. [28] and Classen et al. [30] found higher compressive stress for refractive indices of about 1.9. In this work, higher SiH_4 flow (57 versus 7 sccm) resulted in higher stress value. Consequently, all these results would also appear to be in agreement.

The observation that PECVD SiO_xN_y films can be deposited with a low compressive stress while having good

Table 4
Overview of measured values of σ_f and E_f reported from the literature

Ref.	Nature of deposition	Stress [MPa]	Young's modulus [GPa]	Refractive index	Pressure [mbar]	Temperature [°C]
Danaie et al. [28]	400 nm on Si wafer	− 330 to − 1050	86–149	1.48–1.9	500	200–300
Kramer and Paul [18]	1.9 μm on Si membrane	− 320	150	1.9–2.0	–	300
Denisse et al. [29]	on Si wafer	− 240 to − 310	–	1.5–1.7	1.45	380
Classen et al. [30]	Si wafer	− 170 to − 780	–	1.51–1.91	0.65	300
Allaert et al. [31]	100 nm on Si wafer	− 180	–	1.85	3.6	220–315
This work	2 μm on Si membrane	− 90 to − 400	78–147	1.51–1.81	0.14	350

control of refractive index makes these layers attractive candidates for application as core layer in channel optical waveguide in MOEMS devices.

Acknowledgements

This work is supported by Growth Programme of the European Union (contract G1RD-CT-2000-00261). L. Nieradko acknowledges the support from Marie Curie Individual Fellowship (contract HPMF-CT-2001-01200). The authors thank Pascal Blind from the Centre de Transfert des Microtechnologies (Besançon, France) for his help in fabrication of samples.

References

[1] C. Gorecki, in: P. Rai-Choudhury (Ed.), MEMS and MOEMS—Technology and Applications, SPIE Press, Bellingham, 2000, p. 209.

[2] W.N. Sharpe Jr., B. Yuan, R. Vaidyanathan, in: M.T. Postek, C. Friedrich (Eds.), Micromachining and Microfabrication '96, Microlitography and Metrology in Micromachining II, Austin, TX, U.S.A., October 14–15, 1996, Proceedings of the SPIE, vol. 2880, International Society for Optical Engineering, Bellingham, WA, 1996, p. 78.

[3] H. Ogawa, K. Suzuki, S. Kaneko, Y. Nakano, Y. Ishikawa, T. Kitahara, The 10th Annual International Workshop on MEMS, Nagoya, Japan, January 26–30, 1997, Proceedings of the IEEE 97CH36021, 1997, p. 430.

[4] P.J. French, P.M. Sarro, R. Mallé, E.J.M. Fakkeldij, R.F. Wolffenbuttel, Sens. Actuators, A, Phys. 58 (1997) 149.

[5] W. Osten, W. Juptner, S. Seebacher, T. Baumbach, in: C. Gorecki (Ed.), Industrial Lasers and Inspection: Microsystems Metrology and Inspection, Munich, Germany, June 14–18, 1999, Proceedings of the SPIE, vol. 3825, International Society for Optical Engineering, Bellingham, WA, 1999, p. 152.

[6] S. Seebacher, W. Osten, T. Baumbach, W. Juptner, Opt. Lasers Eng. 36 (2001) 103.

[7] S. Petitgrand, R. Yahiaoui, K. Danaie, A. Bosseboeuf, J.P. Gilles, Opt. Lasers Eng. 136 (2000) 77.

[8] P. Aswendt, R. Hofling, K. Hiller, in: C. Gorecki (Ed.), Industrial Lasers and Inspection: Microsystems Metrology and Inspection, Munich, Germany, June 14–18, 1999, Proceedings of the SPIE, vol. 3825, International Society for Optical Engineering, Bellingham, WA, 1999, p. 165.

[9] V. Petrov, B. Lau, in: M. Kujawinska, W. Osten (Eds.), Industrial Lasers and Inspection: Optical Measurement Systems for Industrial Inspection, Munich, Germany, June 14–18, 1999, Proceedings of the SPIE, vol. 3824, International Society for Optical Engineering, Bellingham, WA, 1999, pp. 262–273.

[10] H. Bezzaoui, E. Voges, Sens. Actuators, A, Phys. 29 (1991) 219.

[11] E. Bonnotte, C. Gorecki, H. Toshiyoshi, H. Kawakatsu, H. Fujita, K. Wörhoff, K. Hashimoto, J. Lightwave Technol. 17 (1999) 35.

[12] C. Poilane, P. Delobelle, C. Lexcellent, S. Hayashi, H. Tobushi, Thin Solid Films 379 (2000) 156.

[13] C. Gorecki, A. Sabac, M. Józwik, S.S. Lee, in: A.K. Asundi, W. Osten, V.K. Varadan (Eds.), ISPA-Photonics and Applications, Advanced Photonics Sensors and Applications II, November 26–30, 2001, Singapore, Proceeding of the SPIE, vol. 4596, International Society for Optical Engineering, Bellingham, WA, 2001, p. 9.

[14] W.C. Oliver, G.M. Pharr, J. Mater. Res. 7 (1992) 1564.

[15] G.M. Pharr, W.C. Oliver, J. Mater. Res. 7 (1992) 613.

[16] M. Józwik, C. Gorecki, A. Sabac, P. Delobelle, M. Kujawińska, Opt. Lasers Eng. 41 (2003) 703.

[17] M. Kujawińska, Automatic fringe pattern analysis, in: K. Patorski (Ed.), Handbook of the Moiré Fringe Technique, Elsevier, Amsterdam, 1993, p. 339.

[18] T. Kramer, O. Paul, J. Micromechanics Microengineering 12 (2002) 475.

[19] M.K. Small, W.D. Nix, J. Mater. Res. 7 (1992) 1553.

[20] O. Tabata, K. Kawabata, S. Sugiyama, I. Igarashi, Sens. Actuators 20 (1989) 135.

[21] E. Bonotte, P. Delobelle, L. Bornier, B. Troland, G.J. Tribillon, J. Mater. Res. 12 (1997) 2234.

[22] S. Hong, T.P. Weihs, T.C. Bravman, W.D. Nix, J. Electr. Mater. 19 (1990) 903.

[23] S. Timoshenko, S. Woinowsky-Krieger, in: Ch. Beranger (Ed.), Théorie des Plaques et Coques, Libraire Polytechnique, Paris, 1961, in French.

[24] D. Maier-Sneider, J. Maibach, E. Obermeier, J. Micromech. Syst. 4 (1995) 238.

[25] L.G. Parrat, Phys. Rev. 95 (1954) 359.

[26] K. Danaie, DSc Thesis, Université Pierre et Marie Curie (Paris VI), France, 2002, in French.

[27] J.J. Vlassak, W.D. Nix, J. Mech. Phys. Solids 42 (1994) 1223.

[28] K. Danaie, A. Bosseboeuf, C. Clerc, C. Gousset, G. Julie, Sens. Actuators, A, Phys. 99 (2002) 78.

[29] C.M.M. Denisse, K.Z. Troost, J.B. Oude Elferink, F.H.P.M. Harbaken, M. Hendriks, J. Appl. Phys. 60 (1986) 2536.

[30] W.A.P. Classen, H.A.J.Th.V.D. Pol, A.H. Goemans, A.E.T. Kuiper, J. Electrochem. Soc. 33 (1986) 1458.

[31] K. Allaert, A. Van Calster, H. Loos, A. Lequesne, J. Electrochem. Soc. 137 (1985) 1763.